Supporting Information

Monolithic metasurface for ultra-stable nuclear spin frequency for miniaturized NMR optical pumping

Yan Xu[a,b,c,d,e], Zhen Chai[a,b,c,d,e,*], Chuqing Sun[a,b,c,d,e], Rui Wang[a,b,c,d,e], Kun Huang[a,b,c,d,e], Jianli Li[a,b,c,d,e,*]

[a]Key Laboratory of Ultra-Weak Magnetic Field Measurement Technology Ministry of Education, School of Instrumentation and Optoelectronic Engineering, Beihang University, Beijing 100191, China

[b]Institute of Large-scale Scientific Facility and Centre for Zero Magnetic Field Science, Beihang University, Beijing 100191, China

[c]Hangzhou Institute of Extremely-Weak Magnetic Field Major National Science and Technology infrastructure, Hangzhou 310051, China

[d]Beihang Hangzhou Innovation Institute, Hangzhou 310052, China

[e]Hefei National Laboratory, Hefei 230088, China

*E-mail: zhenchai@buaa.edu.cn; lijianli@buaa.edu.cn

Table of contents

Section 1. Meta-atom Parameter Scanning Results

We set the meta-atom period to 400 nm with a height of 450 nm, using amorphous silicon as the material. To explore the effects of elliptical nanopillar geometry on the optical response, we systematically varied the semi-axis lengths R_1 and R_2 of the elliptical nanopillars within the range of 40-180 nm, with a step size of 2 nm between adjacent scanning parameters. We then simulated the transmitted light propagation, phase response, and polarization characteristics using the FDTD method. Periodic and perfectly matched layer boundary conditions were applied along the transverse and longitudinal directions, respectively.

The incident light frequency was selected to match the D1 line of ^{87}Rb. The R_1 axis of the elliptical nanopillars was oriented at 45° relative to the x-axis. For illumination, we used x-polarized light to interact with the metasurface. The phase of the transmitted x- and y-polarized components, as well as their phase difference, are shown in **Fig. S1a–c**. These results provide insight into how the metasurface manipulates the phase of the transmitted light in response to the varying geometry of the nanopillars. Further, we evaluated the polarization control characteristics of the metasurface by analyzing the DOCP, the polarization ellipse orientation angle, and the amplitude ratio between the x- and y-polarized components. These results, shown in **Fig. S1d–f**, reveal how the structural parameters of the metasurface influence its ability to generate and control various polarization states.

The transmittance of RCP light, LCP light, and the total transmittance are shown in **Fig. S1g-i**.

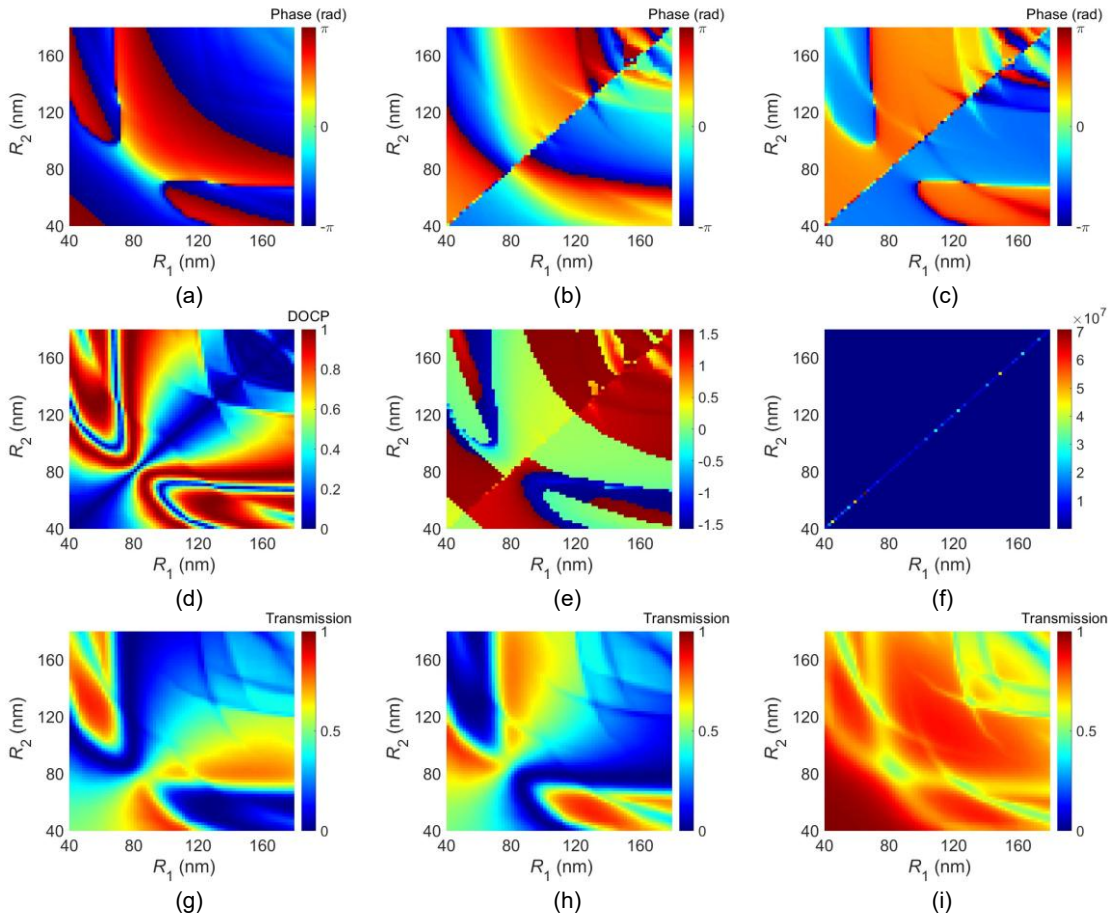

Fig. S1. Parameter scanning results. Phase of the transmitted (a) x-polarized component, (b) the y-polarized component and (c) phase difference between them. (d) DOCP of the transmitted light. (e) Polarization ellipse orientation angle. (f) Amplitude ratio between x- and y-polarized components. Transmittance of (g) RCP light; (h) LCP light and (i) total of them.

To achieve metasurface unit cells capable of collimating and circularizing light, two key conditions must be met: the DOCP of the transmitted light should be as close to 1 as possible; the phase of the x-polarized component should cover a full 0-2π range. Based on these requirements and practical fabrication constraints, the structural parameters of the selected meta-atom database are summarized in **Table S1.**

Table S1 Structural parameters of the selected meta-atom database.

Number	1	2	3	4	5	6	7	8	9	10	11
R_1 (nm)	58	62	86	84	86	88	90	96	120	144	168
R_2 (nm)	124	128	60	72	74	76	78	78	76	76	78

Section 2. Optical performance simulation

Fig. S2a and **S2b** show the collimation phase distribution and corresponding meta-atom arrangement for a lens with a diameter of 60 μm and a focal length of 227.87 μm, maintaining the same NA as the final fabricated sample. Since focusing and collimation are reversible processes, we used the focusing process as a validation method. We simulated the response of the metasurface to an x-LP plane wave. The 2D focal spot is shown in **Fig. S2c**. The normalized transverse intensity profile reveals a FWHM of 2.66 μm approximately 0.44λ/NA for the focal spot, as shown in **Fig. S2d**, indicating that the focusing performance is near the diffraction limit, with excellent beam focusing quality.

To investigate the relationship between the output DOCP, the incident laser polarization angle, and the metasurface orientation, we simulated the DOCP under varying incident polarization directions. As shown in **Fig. S2e**, the DOCP exhibits a sinusoidal variation between 0 and 1, consistent with the behavior of an ideal QWP. **Fig. S2f** presents the phase difference and amplitude ratio between the x- and y-polarized components of the output light. The phase difference varies linearly with the incident polarization angle, covering a complete 2π range, while the amplitude ratio follows a sinusoidal trend, remaining within 1 ± 0.01. The polarization state evolution under composite rotation operations is illustrated on the Poincaré sphere in **Fig. S2g**, displaying a figure-eight trajectory that transitions through linear, elliptical, and circular polarization states. The polarization conversion efficiency dependence on the incident polarization angle aligns well with theoretical predictions. This versatile polarization control capability provides enhanced design flexibility for optical pumping systems in NMR co-magnetometers, enabling optimized spin polarization through tunable light-matter interactions.

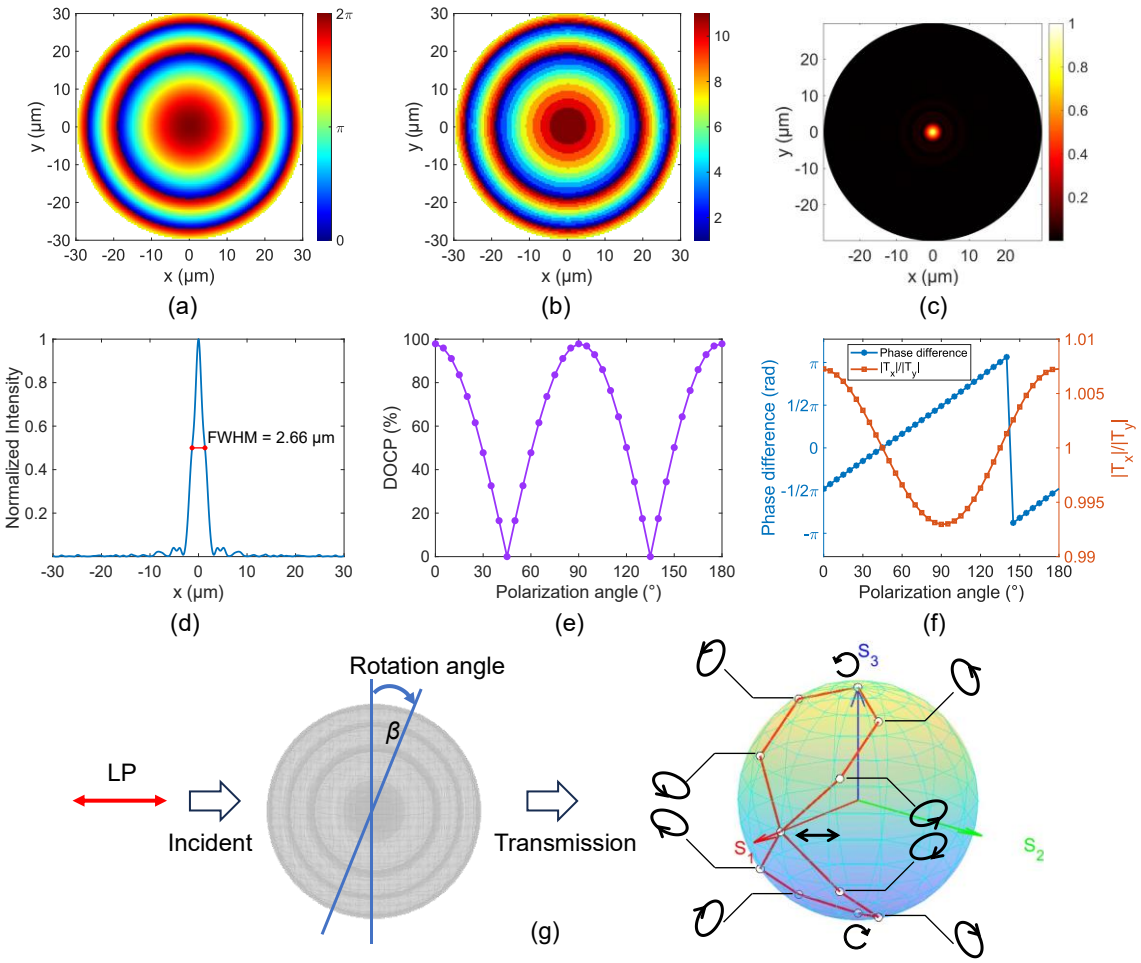

Fig. S2. Optical performance simulation. (a) Phase distribution of the small-scale metasurface. (b) Corresponding meta-atom arrangement. (c) 2D focal spot at the focal plane. (d) Normalized transverse intensity distribution and FWHM of the focal spot. (e) DOCP of the output light as a function of incident polarization angle. (f) Phase difference and amplitude ratio between x- and y-polarized components under different incident polarization angles. (g) Trajectory of the output polarization state on the Poincaré sphere under composite rotation operations.

Section 3. Analysis of the Influence of NA and Clear Aperture Size on Phase-Polarization Modulation Performance

To comprehensively evaluate the scalability of our metasurface design, we systematically investigated the effects of NA and clear aperture size on both focusing performance and polarization conversion efficiency. Our simulations demonstrate successful implementation of both collimation and focusing functions across a wide NA range from 0.2610 to 0.6525 (five times the target value), as shown in **Fig. S3**. While varying the clear aperture diameter with a constant NA=0.1305, **Fig. S4** presents the focusing characteristics for aperture sizes ranging from 20 μm to 50 μm. The axial propagation patterns and focal plane intensity distributions maintain excellent beam quality throughout this NA and aperture range, with the 1D and 2D intensity profiles showing well-defined focal spots. However, quantitative analysis reveals an important trade-off: while higher NA values enable stronger light confinement, as evidenced by decreasing FWHM in **Fig. S5a**, they also lead to gradual degradation of polarization purity.

The observed decrease in DOCP with increasing NA originates from fundamental wavefront engineering constraints. A higher NA requires a steeper spatial phase gradient, which our discrete meta-atom library, which includes 11 elements with phase steps $\leqslant \pi/5$ must approximate through sampling. This discretization introduces local phase errors that degrade the coherent superposition of orthogonal polarization components, directly reducing DOCP. Moreover, the dual-function requirement of simultaneously satisfying the quadratic phase profile for focusing and the quarter-waveplate condition forces the meta-atoms to operate near their design limits. As the phase gradient steepens, local deviations in the phase difference $\Delta\varphi$ from the ideal $\pi/2$ become more pronounced, further compromising polarization purity. Despite this trade-off, the performance degradation remains manageable. Even when NA is increased fivefold from 0.1305 to 0.6525, the DOCP remains above 92%, demonstrating the robustness of our design methodology.

For high-NA applications requiring both strong focusing and high polarization purity, several strategies could mitigate this degradation. Expanding the meta-atom library with finer phase steps would reduce sampling errors at the expense of design complexity. Inverse design approaches could optimize meta-atom geometries beyond predefined library constraints, enabling superior simultaneous control of phase and polarization. From a materials perspective, higher-index dielectrics could enhance light confinement and reduce scattering losses. Notably, for our target application of NMR optical pumping, the required NA is

modest (0.1305), and even at five times this value, the DOCP remains above 92%, which is still acceptable for many atomic sensing applications. As shown in **Fig. S5b**, DOCP stays above 97% across varying aperture sizes, while FWHM exhibits expected diffraction-limited variations.

These findings provide practical guidance for tailoring metasurface parameters to specific beam quality and polarization fidelity requirements. The minimal variation of DOCP with aperture size confirms that millimeter-scale metasurfaces retain polarization performance comparable to small-scale simulations, supporting scalability toward future sub-millimeter vapor cell technologies. The NA-dependent DOCP degradation underscores the need for careful balance between focusing strength and polarization purity in high-NA applications.

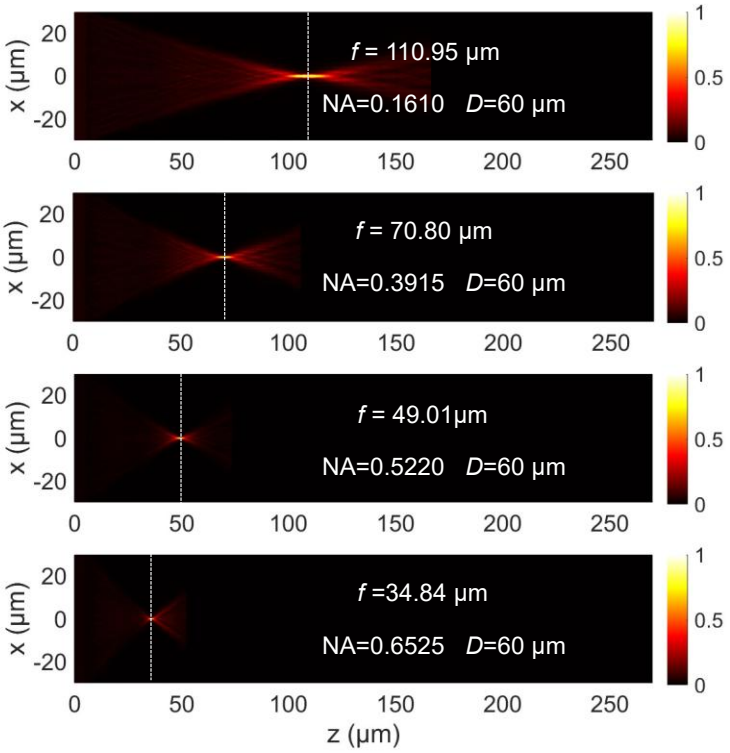

Fig. S3. Metasurface focusing characteristics under varying NA settings with constant clear aperture diameter D=60 μm, showing axial propagation patterns.

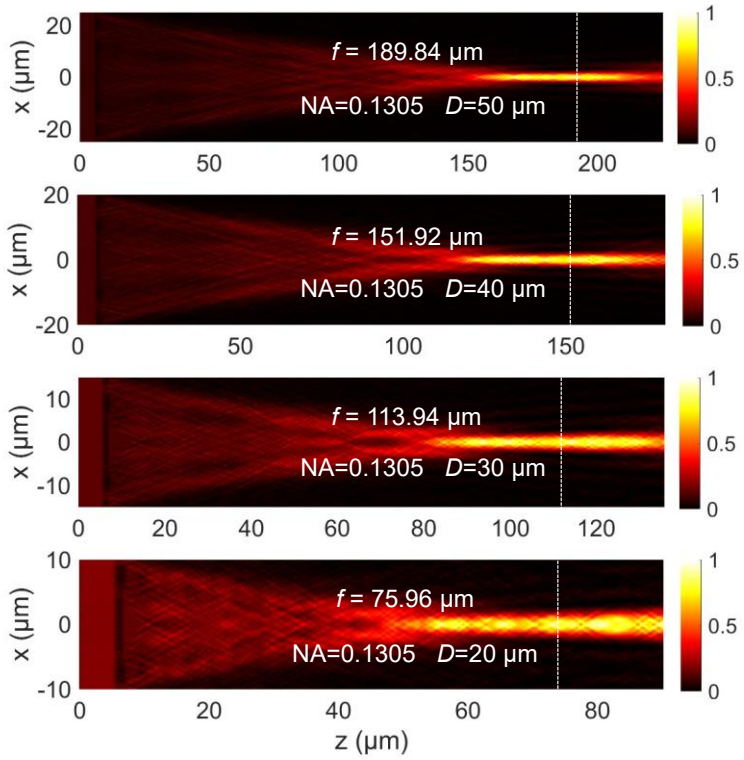

Fig. S4. Metasurface focusing characteristics under different clear aperture diameter settings with constant NA=0.1305, showing axial propagation patterns.

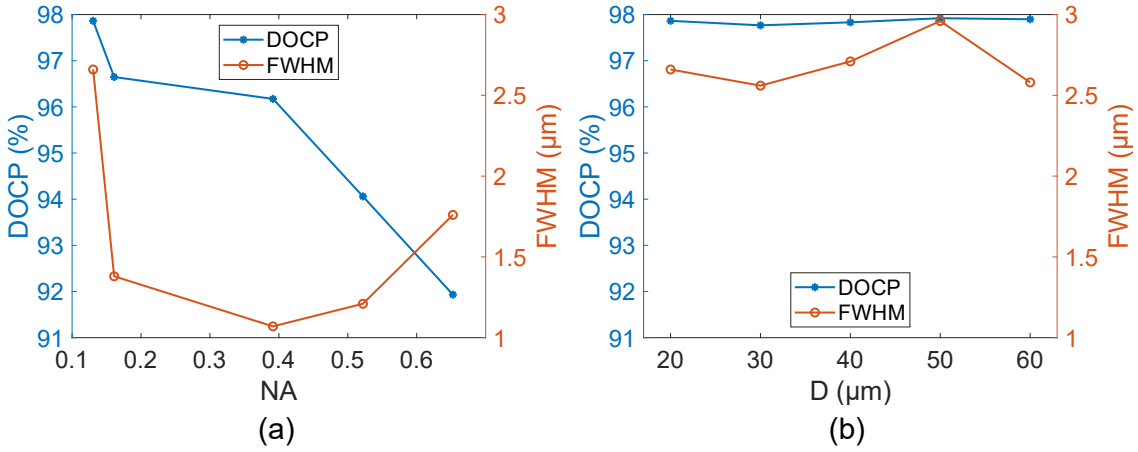

Fig. S5. Quantitative comparison of (a) NA-dependent and (b) aperture-dependent DOCP and FWHM performance.

Section 4. Sample Fabrication

The silicon metasurface sample was fabricated on a 500 μm SiO_2 substrate, featuring a clear aperture of 3.2 mm with a designed focal length of 8.73 mm, as shown in **Fig. S6a**. First, a double-polished fused silica substrate with a thickness of 500 μm was inspected and cleaned to ensure a contamination-free surface. A 450 nm thick amorphous silicon film was then deposited using ion-assisted deposition (IAD), targeting a refractive index of 3.76 ± 0.01 and an extinction coefficient of 0.039 ± 0.01 at a wavelength of 795 nm. Next, a 200 nm layer of electron beam resist (ZEP520A) was spin-coated onto the silicon film and baked. The metasurface pattern was exposed via EBL at an acceleration voltage of 100 kV with a dose of 150 μC/cm² and an electron beam current of 2 nA, optimized to achieve high-resolution patterning and faithful resist profiles. After development, a 50 nm Cr hard mask was deposited via electron beam evaporation, followed by a lift-off process to define the mask structure. Inductively coupled plasma (ICP) etching was then employed to transfer the pattern into the 450 nm silicon layer. Etching depth uniformity was controlled through a two-step strategy. First, high-resolution patterning was achieved using EBL, which established an excellent foundation for subsequent etching. Second, the etching process itself was carefully optimized. This involved iterative pre-fabrication tests to determine the optimal gas mixture and plasma parameters for the ICP step. This systematic calibration allowed us to achieve a consistent etch depth of 450 nm with a thickness tolerance maintained within 5% of the target value. Subsequently, the residual Cr mask was chemically removed. Finally, the wafer was diced into a 1 cm × 1 cm chip. The fabricated elliptical nanopillar arrays were characterized by scanning electron microscopy (SEM). **Fig. S6b** and **S6c** show the top and side views, respectively, confirming excellent morphological quality and precise subwavelength structural control.

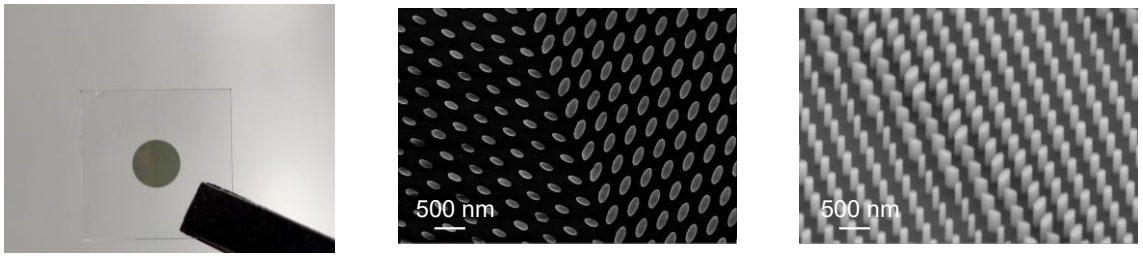

Fig. S6. Characterization of sample morphology. (a) Optical image of the sample with 3.2 mm clear aperture. (b) Top-view and (c) side-view SEM images of local structures.

Section 5. Stokes Parameters and Spot Polarization States Measurement

The continuously tunable DOCP, normalized Stokes parameters and ellipticity of the emitted light, as shown in **Fig. S7a-c**, were measured as the metasurface was rotated 180 degrees. This highlights the sample's ability to control all polarization states. Furthermore, for spatially resolved polarization analysis, we developed a rotating-waveplate Stokes polarimetry system consisting of a linear polarizer and a QWP, as shown in **Fig. S8**. This system utilizes high-precision displacement stages, including Thorlabs MBT402D/M, MBT616D/M, and XR25P-K1/M along with a Thorlabs BC207VIS beam profiler are set for intensity distribution mapping.

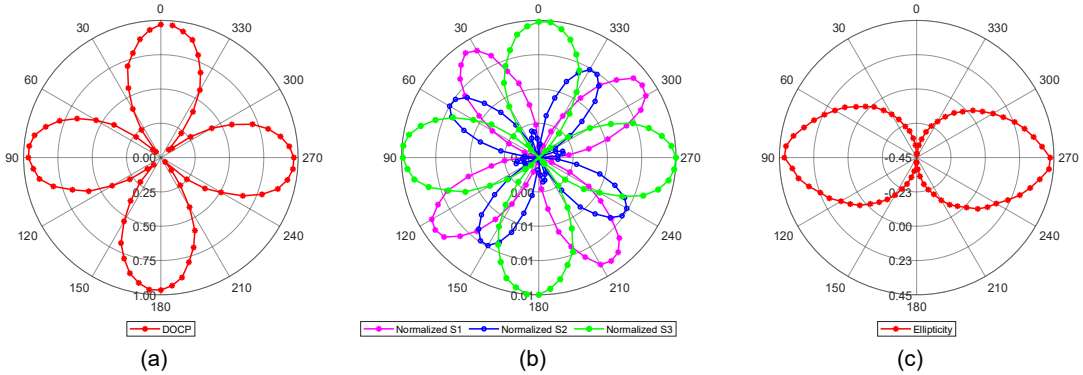

Fig. S7. Characterization of polarization conversion performance. (a) DOCP variation, (b) normalized Stokes parameters, and (c) ellipticity as the metasurface is rotated 180° for polarization control.

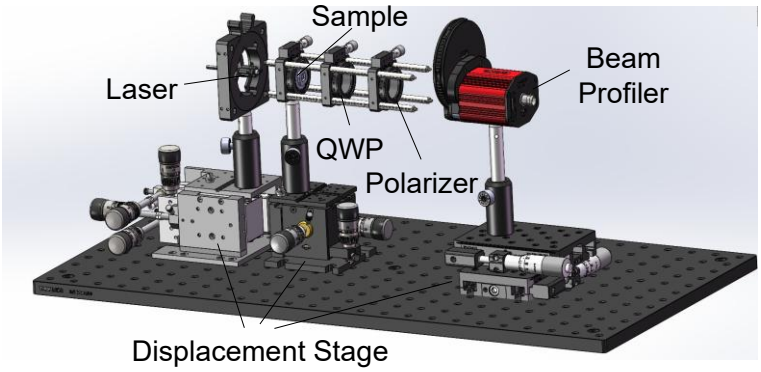

Fig. S8. Optical setup for 2D Stokes parameter measurements.

Fig. S9 illustrates the experimental configurations for measuring the four intensity distributions. Initially, a linear polarizer was inserted into the optical path, followed by recording the intensity distribution of the transmitted light spot when the transmission axis was aligned horizontally, vertically, and at +45°. These three intensity distributions were used to calculate the first three Stokes parameters. To obtain the fourth Stokes parameter, we

inserted a QWP with its fast axis aligned horizontally in front of the 45° linear polarizer. After measuring the intensity distribution of the transmitted light spot, the fourth Stokes parameter was calculated.

The Stokes parameters, composed of four components, fully describe the polarization state of light. The calculation formulas are as follows:

$$\begin{cases} S_0 = I_1(0^0) + I_2(90^0) \\ S_1 = I_1(0^0) - I_2(90^0) \\ S_2 = 2I_3(45^0) - S_0 \\ S_3 = S_0 - 2I_4(0^0, 45^0) \end{cases}, \tag{S1}$$

where S_0 represents the total intensity of the light, S_1 is the difference between the intensity of horizontally and vertically PL, S_2 is the difference between the intensities of +45° and -45° PL, and S_3 is the difference between the intensities of RCP and LCP light.

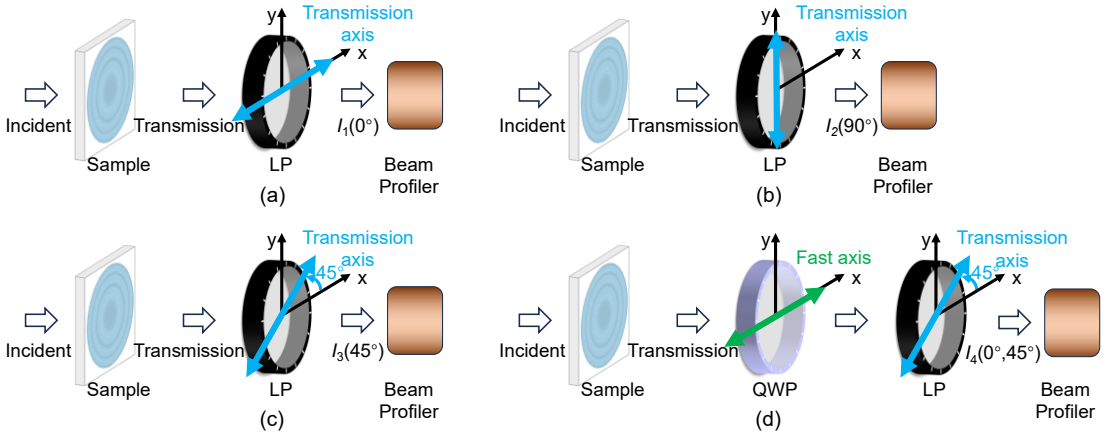

Fig. S9. Experimental setup for 2D Stokes parameters and spot polarization states measurement. (a) I_1(0°); (b) I_2(90°); (c) I_3(45°); and (d) I_4(0°,45°).

Additionally, the DOCP and degree of linear polarization (DOLP) can be expressed as:

$$\mathrm{DOCP} = \frac{I_{circular}}{I_{tot}} = \frac{S_3}{S_0}, \tag{S2}$$

$$\mathrm{DOLP} = \frac{I_{linear}}{I_{tot}} = \frac{\sqrt{S_1^2 + S_2^2}}{S_0}, \tag{S3}$$

where I_{tot} is the total intensity of the transmitted light, and $I_{circular}$ and I_{linear} are the CP and LP components of the transmitted light, respectively.

Fig. S10 presents the spatial distributions of the measured Stokes parameters, DOCP, and DOLP for the output beam at every 22.5° rotation angle, demonstrating comprehensive polarization-state manipulation capabilities. The observed polarization control versatility, as

evidenced by these results, enables precise manipulation of light-matter interactions - a critical requirement for advanced quantum sensing implementations.

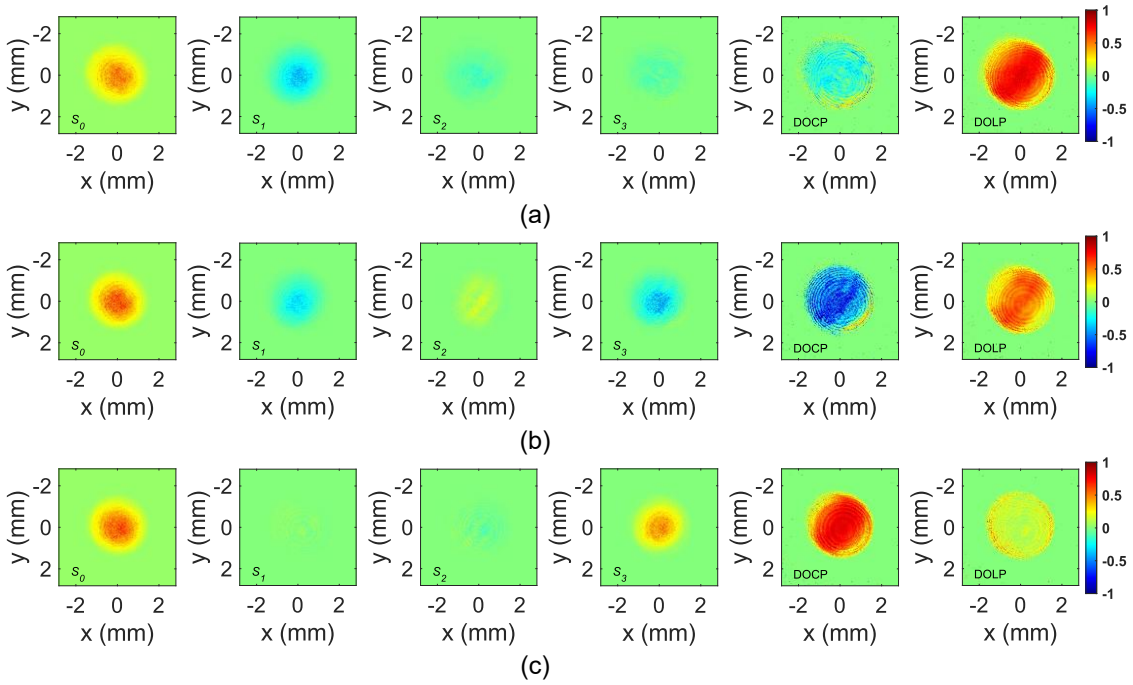

Fig. S10. Spatial distributions of the Stokes parameters, DOCP, and DOLP of the output beam at rotation angles of (a) 0°; (b) 22.5°; and (c) 45°.

Section 6. DOCP of Different Laser Frequencies

Fig. S11 shows the DOCP of the emitted light at different incident laser frequencies. Within the ±200 GHz range of the D1 line, the DOCP consistently exceeds 94.5%, meeting the tuning requirements of the NMR co- magnetometer pumping system.

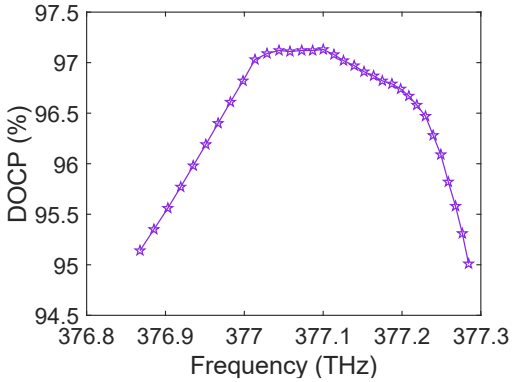

Fig. S11. DOCP as a function of laser frequency detuning.

Section 7. Focusing Performance Characterization

The experimental setup for evaluating the focusing performance is illustrated in **Fig. S12a**. A collimated beam with a diameter of 2.3 mm was normally incident on the metasurface sample. The focused beam profile was characterized using a Mitutoyo 100X infinity-corrected plan apochromat objective (NA=0.55, working distance=13.0 mm, focal length=2 mm) coupled with a tube lens, with the focused beam captured by a beam profiler. Precise positioning of the sample, objective lens, tube lens, and beam profiler was achieved using displacement stages. **Fig. S12b** shows the transmitted beam profiles at propagation distances of 0, 4, 8, 12, 16, and 20 mm, demonstrating the beam evolution toward the focal plane. The complete beam propagation along the optical axis, acquired at 10 μm intervals, is presented in **Fig. S12c**. Clear focusing is observed at the focal position of 8.80 mm, with a deviation of only 0.8% from the theoretical focal length. The one-dimensional intensity distributions along x- and y-directions at the focal plane are plotted in **Fig. S12d**, revealing symmetric focusing performance. **Fig. S12e** quantitatively shows the beam diameter variation in both x- and y-directions, as well as the average beam diameter, during axial propagation. This comprehensive characterization confirms the metasurface's ability to achieve focusing at the predetermined focal length while maintaining excellent beam quality. The symmetric intensity profiles and consistent beam waist evolution demonstrate precise control over the wavefront manipulation.

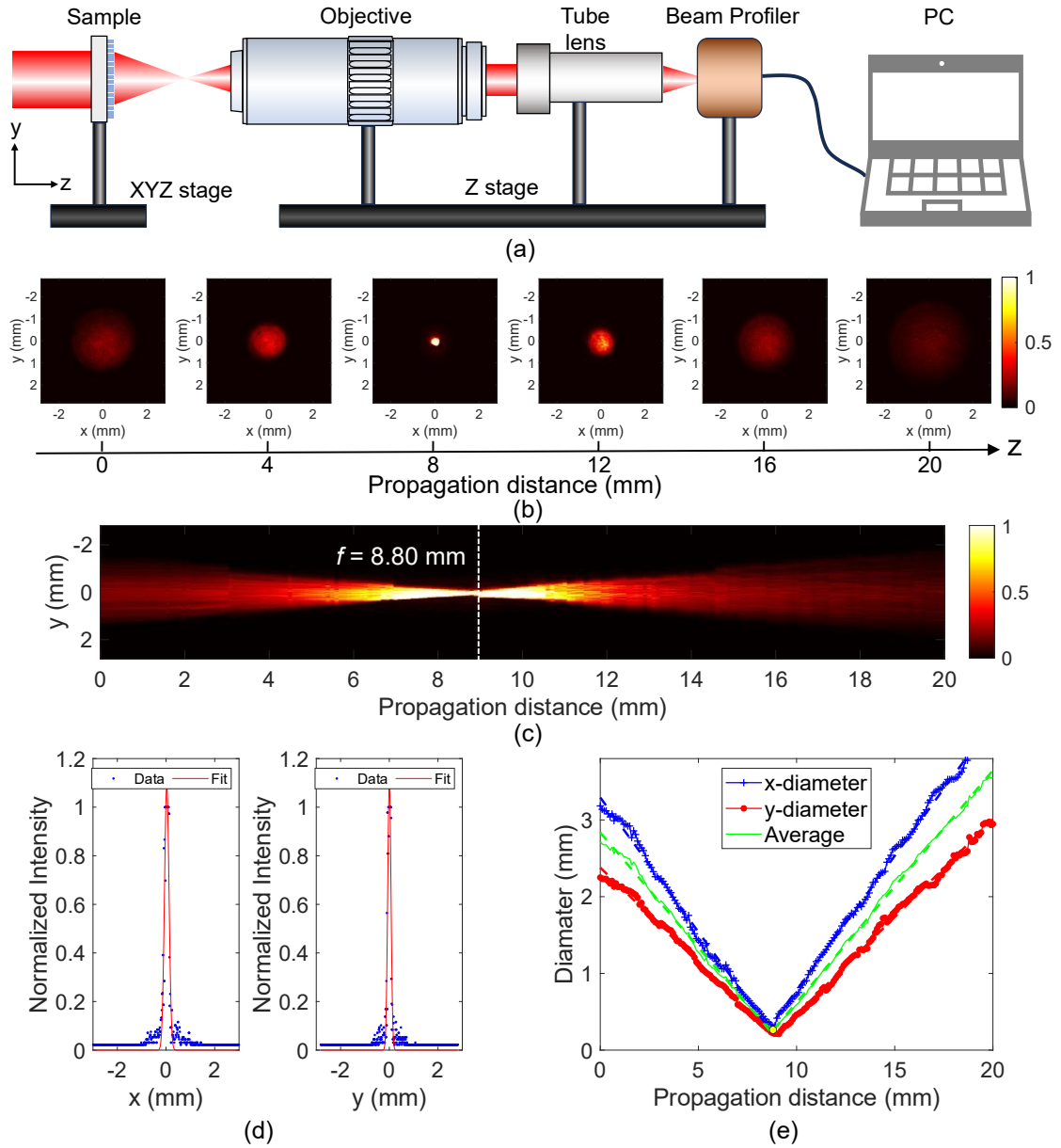

Fig. S12. Focusing Performance. (a) Experimental setup for focusing test. (b) Measured beam profiles along the optical axis of 0, 4, 8, 12, 16, and 20 mm. (c) Beam propagation along the optical axis over 20 mm. (d) Intensity distribution along x- and y-directions at the focal plane. (e) Measured beam diameter variation curve over a 20 mm propagation distance.

To further accurately assess this performance, we have established a quantitative correlation between the measured divergence half-angle of 4.06 mrad and the actual focusing tolerance. For an incident beam with a waist radius of ω_0, after passing through a thin lens with focal length f, the new far-field divergence half-angle θ' is given by:

$$\theta' = \frac{\lambda}{\pi\omega_0} = \frac{\lambda}{\pi}\sqrt{\frac{1}{\omega_0^2}\left(1-\frac{z}{f}\right)^2 + \left(\frac{z_R}{f\omega_0}\right)^2}, \tag{S4}$$

Where λ=795 nm is the operating wavelength, z is the axial distance from the beam waist to the lens plane, $z_R = \frac{\pi\omega_0^2}{\lambda}$ is the Rayleigh length. It can be seen that the closer the incident beam waist is to the focal point of the lens, the smaller the new far-field divergence half-angle becomes.

When the waist is exactly located at the front focal plane of the lens, the divergence half-angle after the thin-lens transformation reaches its minimum:

$$\theta'_{(min)} = \frac{\lambda}{\pi\omega'_{0(max)}} = \frac{\omega_0}{f}. \quad \text{(S5)}$$

This limit corresponds to the case where the output beam approximates a plane wave. At this point, the best achievable collimation performance of the system is directly determined by the incident waist radius ω_0 and the lens focal length f.

In this experiment, the VCSEL laser used has a far-field divergence half-angle of θ=7.5°. Hence, the waist radius and the Rayleigh length are calculated as: ω_0=1.933 μm and z_R=14.765 μm.

A metasurface lens with focal length f as 8.80 mm was employed for collimation. If the VCSEL waist were precisely positioned at the focal point, the theoretically achievable minimum divergence half-angle would be $\theta'_{(min)}$=0.22 mrad. The actually measured divergence half-angle is 4.06 mrad. This discrepancy arises from several practical constraints inherent to our co-optimized, dual-function metasurface. The measured divergence exceeding the diffraction-limit arises from several practical constraints inherent to our co-optimized metasurface design. Simultaneous fulfillment of both the collimation phase map and a quarter-waveplate retardation profile inherently limits available phase resolution and introduces wavefront errors. Further deviations stem from the discrete nature of our meta-atom library combined with fabrication tolerances, which slightly degrade the ideal phase front.

Additionally, the VCSEL source used exhibits inherent divergence, while finite-aperture effects and residual alignment uncertainties contribute to the overall divergence observed after collimation. From the measured value 4.06 mrad, the deviation of the actual waist position from the ideal focal plane is estimated to be about 0.273 mm, which is of the same order as the VCSEL chip height 0.16 mm. This deviation likely originates from alignment tolerances between the chip package and the optical axis, falling within typical assembly variations. Further reduction of this deviation would bring the divergence angle closer to the theoretical minimum, but would require more precise mechanical adjustment and positioning.

Despite exceeding the ideal diffraction limit, the achieved divergence is fully sufficient for uniform optical pumping within the millimeter-scale vapor cell. For an inner cell diameter of 3 mm, a divergence half-angle of 4.06 mrad results in a beam-radius expansion of only 12 μm over the cell length, negligible relative to the cell dimensions. This performance represents a well-balanced outcome of our multi-objective design, which concurrently prioritizes high DOCP, a usable beam diameter, and system-level integrability.

Section 8. Optical Power Efficiency

Optical power measurements were conducted using a Thorlabs PM400 power meter with an S120C photodiode sensor. As shown in **Fig. S13a**, the system achieved an efficiency of 58.07% at the ^{87}Rb D1 line, with long-term power fluctuations maintained below ±1.2% over 1800 s. **Fig. S13b** demonstrates that the efficiency remained stable, ranging between 56% and 60%, across ±200 GHz frequency detuning. All output power measurements were conducted at 12 mm from the metasurface. The experimental results demonstrate excellent agreement between the collimating-polarizing metasurface's performance and theoretical predictions.

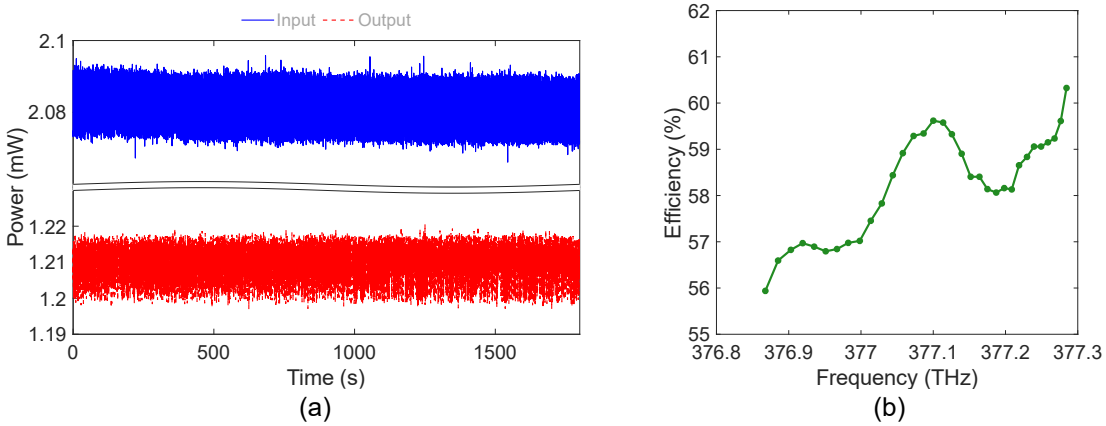

Fig. S13. Optical power efficiency. (a) Long-term stability of input and output power. (b) Collimation efficiency versus laser frequency detuning, with output power measured at 12 mm propagation distance.

Section 9. NMR Optical Pumping Experimental Setup

The experimental setup of the NMR optical pumping based on phase-polarized multiplexed metasurface is shown in **Fig. S14**.

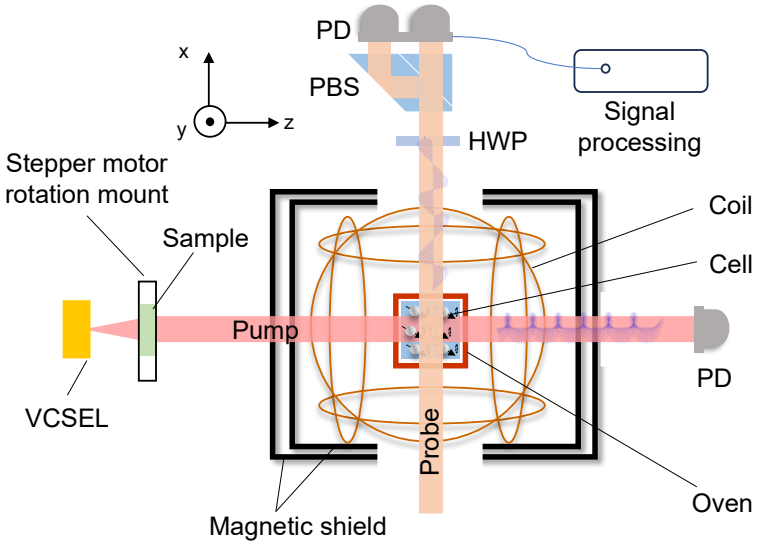

Fig. S14. Phase-Polarization Multiplexed Metasurface for NMR optical pumping experimental setup. PD: photodetector; HWP: half-wave plate.

The laser's electro-optic characteristics are tuned to ensure the pumping light centered around the ^{87}Rb D1 line propagates along the z-axis. To achieve this precise optical control, we first conducted a systematic investigation of the VCSEL's electro-optical properties under varying temperature and injection current conditions. **Fig. S15a** presents the power-current characteristics at different temperatures, with the inset showing detailed measurements near the threshold region. The threshold current exhibits a stable range of 0.7 to 1 mA across the temperature span of 35°C to 70°C. Frequency tuning measurements in **Fig. S15b** showed a consistent monotonic red-shift of emission frequency with increasing injection current at all tested temperatures, providing a predictable linear tuning range for precise frequency control. As shown in **Fig. S15c**, analysis of current tuning efficiency demonstrated that the absolute value of the current tuning coefficient increased with temperature, with higher temperatures significantly enhancing the frequency shift per unit current change, reaching 0.1373 THz/mA at 70°C. This temperature-dependent tuning efficiency must be considered for precise frequency control. For practical application in atomic sensing experiments, particularly for addressing the ^{87}Rb D1 line, the VCSEL frequency can be precisely adjusted through fine current tuning. This characterization provides essential data for implementing both current-based frequency tuning and temperature-assisted frequency stabilization schemes. For atomic

sensing experiments targeting the ^{87}Rb D1 line specifically, this enables precise VCSEL frequency adjustment through fine current tuning while accounting for thermal effects.

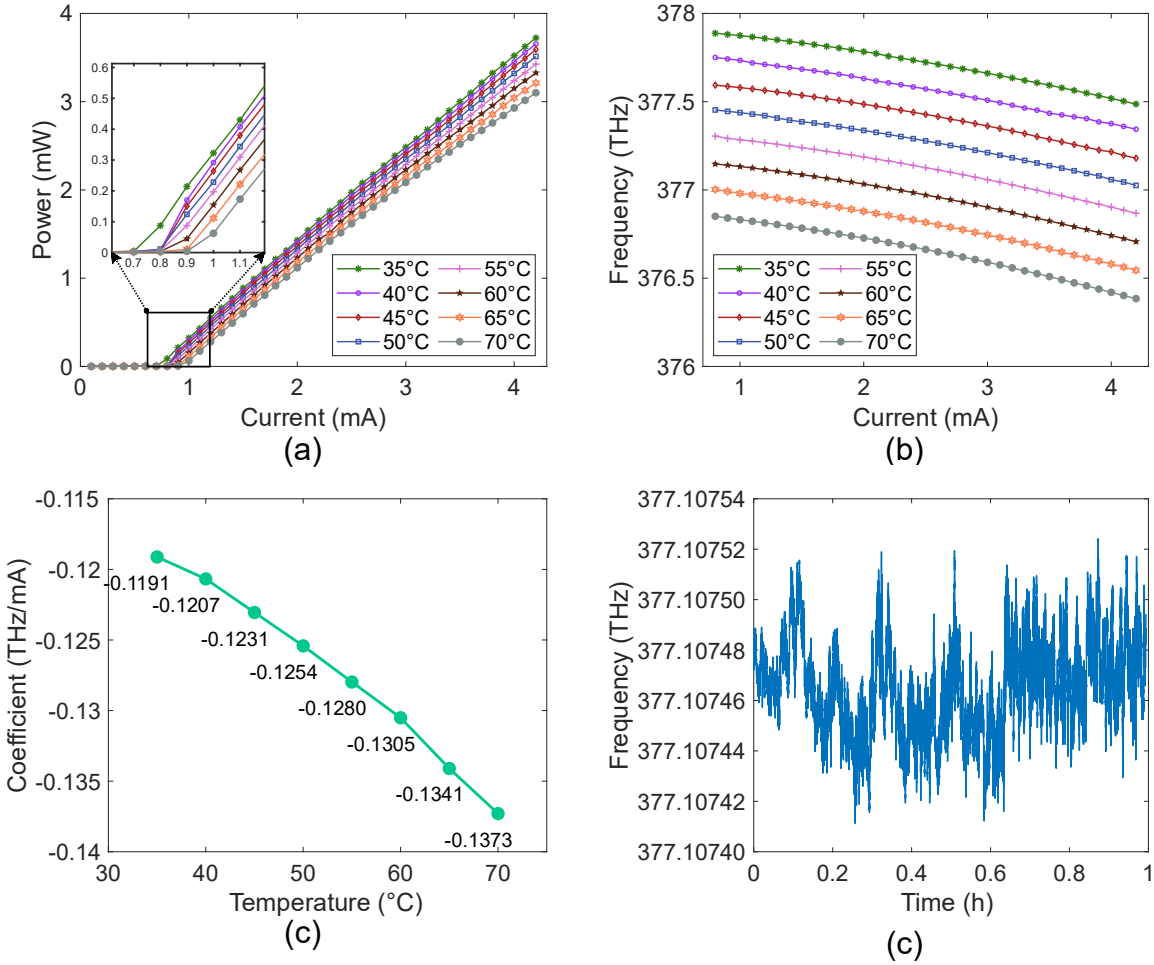

Fig. S15. VCSEL electro-optical characterization. (a) Power-current curves at different temperatures with the inset showing detailed measurements near the threshold region. (b) Frequency-current tuning characteristics at different temperatures. (c) Temperature dependence of current tuning coefficients. (d) Frequency stability over a one-hour period under standard operating conditions.

Building upon this electro-optical characterization, we further assessed the long-term frequency stability of the VCSEL under operating conditions relevant to our NMR experiments. To quantify the frequency stability of the VCSEL source used in our NMR experiments, we monitored its emission frequency over a one-hour period under our standard operating conditions. As shown in **Fig. S15d**, the VCSEL exhibits a peak-to-peak frequency drift of less than 0.11 GHz, with a frequency fluctuation standard deviation of 1.8×10^{-5}. Combining this frequency stability characterization with the DOCP spectral response

presented in **Fig. S11**, we estimate the corresponding DOCP variation induced by such frequency drift to be less than 0.1%, while the absolute DOCP value remains consistently above 97.1%. This confirms that the laser frequency fluctuations have a negligible effect on the output polarization state, ensuring robust and stable circular polarization under realistic operating conditions.

Section 10. Atomic Polarization and Relaxation Rate Measurement

We tested the electronic signal response scanned within the frequency range of 60-90 kHz. **Fig. S16a** shows the periodic variation of electron resonance signals under x-axis RF fields within the range of 0-180°, with maximum response at the ^{87}Rb Larmor frequency. **Fig. S16b** illustrates that the resonance amplitude decreases with reducing DOCP, confirming the critical dependence of electron spin polarization on pumping light polarization state. This behavior aligns with Bloch equation predictions, validating the understanding of the spin dynamics.

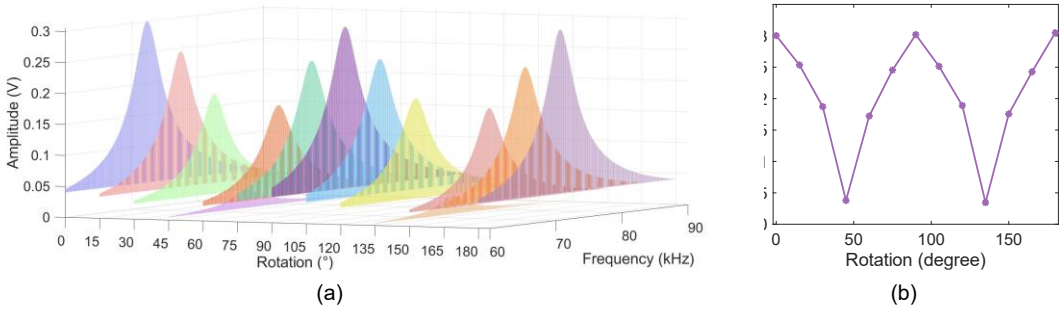

Fig. S16. (a) Electron resonance signals. (b) Resonance amplitude versus rotation angle.

To measure the electron polarization rate, we employed a stepper motor rotation stage to switch the pumping light between RCP and LCP polarization. The alkali metal electron spin polarization P_{Rb} was then determined by measuring the resultant shift in noble gas atomic resonance frequency $\Delta\nu_{\mathrm{Xe}}$ before and after this polarization reversal:

$$\Delta\nu_{\mathrm{Xe}} = 2\gamma_{\mathrm{Xe}}B_{\mathrm{Rb}} = 2\gamma_{\mathrm{Xe}} \cdot \frac{2}{3}\kappa_0\mu_0\mu_B g_s n_{\mathrm{Rb}} \cdot \frac{1}{2}P_{\mathrm{Rb}}, \qquad \text{(S6)}$$

where γ_{Xe} represents the gyromagnetic ratio of Xe, κ_0 is the enhancement factor for Rb-^{129}Xe coupling, μ_0 denotes the permeability of free space, μ_{B} stands for the Bohr magneton, g_s corresponds to the electron g-factor, and n_{Rb} represents atomic number density of Rb in the vapor cell.

The spin polarization and transverse relaxation rate of noble gas atoms were measured using the FID method. A π/2 resonant magnetic pulse was applied along the x-axis to the noble gas atoms, with the FID signal being acquired through an NI DAQ card. Since the pumping light propagates along the z-axis, the spin magnetic moment of the noble gas atoms also aligns with the z-direction, exhibiting no projection in the x-y plane. When a magnetic field is present in the x-y plane, it causes the noble gas atomic spins to deviate from the z-axis, thereby generating a measurable projection in the x-y plane that manifests in the detection signal. The FID decay curve was fitted with an exponential function $f(t)=Ae^{-t/\tau}$, from which

we extracted both the transverse relaxation time and relaxation rate. The noble gas spin polarization P_{Xe} was calculated from the initial amplitude V_{FID} of the FID signal according to:

$$V_{\mathrm{FID}} = K \cdot B_{\mathrm{Xe}} = K \cdot \frac{2}{3}\kappa_0\mu_0\mu_{\mathrm{Xe}}n_{\mathrm{Xe}}P_{\mathrm{Xe}}, \tag{S7}$$

where μ_{Xe} is the magnetic moment of Xe, and n_{Xe} is the number density of Xe. K represents the in-situ magnetometer scale factor obtained from calibration signals, showing the relationship between the magnetic field perceived by the atoms and the output signal.

Section 11. Nuclear Transverse Relaxation Rates

The measured relaxation rates show remarkable consistency between both approaches, as quantitatively summarized in **Table S2.**

Table S2 Comparison of nuclear transverse relaxation rates for different pumping configurations.

Configuration		^{129}Xe (RCP)	^{129}Xe (LCP)	^{131}Xe (RCP)	^{131}Xe (LCP)
Relaxation rates (s^{-1})	Conventional setup	0.07837	0.05664	0.09048	0.09608
	Metasurface setup	0.07913	0.05548	0.08964	0.09778
Relative difference		0.97%	-2.05%	-0.93%	1.77%

Section 12. Independent Long-Term Stability Tests

To ensure the reliability and reproducibility of our long-term stability measurements, we conducted three independent 3-hour stability tests under identical experimental conditions. All three independent tests followed the same experimental protocol and the NMR co-magnetometer system was operated under identical thermal conditions with precise vibrational isolation. Each 3-hour continuous measurement recorded the precession frequencies of both ^{129}Xe and ^{131}Xe nuclei, as shown in **Fig. S17**, enabling computation of the corresponding spin precession frequency error f_{error}. The complete dataset from all three tests demonstrates remarkable consistency in frequency stability performance.

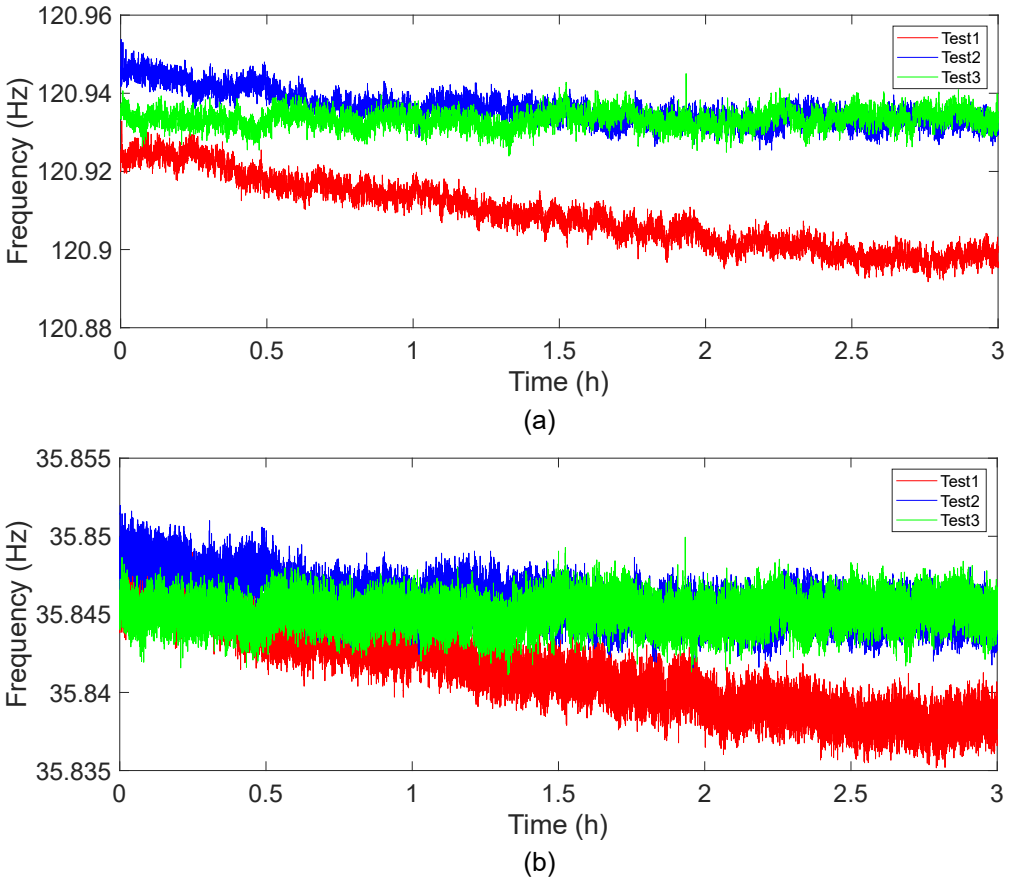

Fig. S17. Precession frequencies of (a) ^{129}Xe and (b) ^{131}Xe.

To further visualize the experimental data, the distributions of the measured f_{error} values from the three test sets were illustrated using box plots, as shown in **Fig. S18**. All measured f_{error} values across individual test instances consistently remained within a stable range of $<$ ±0.009 Hz, confirming the high reproducibility of the measurements. The box plot analyses reveal that the means and distributions from each run are closely aligned, indicating superior measurement stability across different experimental trials. This comprehensive triplicate validation method provides strong evidence for the system's reliability and consistency over

multiple operational cycles. The minimal performance variations observed between independent test runs effectively address potential concerns regarding performance degradation, validating the scalability of the metasurface-integrated technology for long-term quantum sensing applications. The consistent results obtained under identical conditions further reinforce the credibility of the stability assessment and underscore the robustness of the integrated metasurface system.

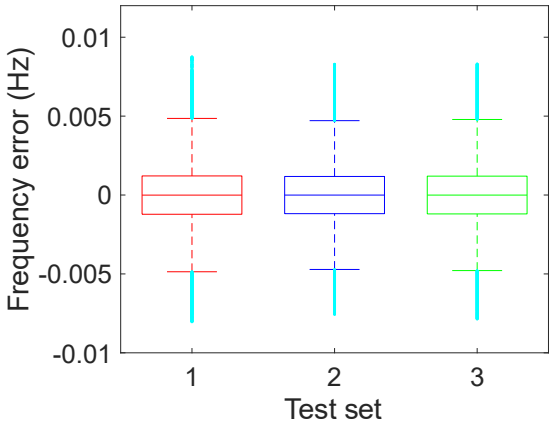

Fig. S18. Three sets of frequency errors between ^{129}Xe and ^{131}Xe.